Chemical Engineering Journal 474 (2023) 145460

Contents lists available at ScienceDirect

Chemical Engineering Journal

journal homepage: www.elsevier.com/locate/cej

CO_2 methanation over LDH derived NiMgAl and NiMgAlFe oxides: Improving activity at lower temperatures via an ultrasound-assisted preparation

Michel Obeid [a,b], Christophe Poupin [a,*], Madona Labaki [b], Samer Aouad [c], François Delattre [a], Sharad Gupta [a], Haingomalala Lucette Tidahy [a], Aida Younis [c], Ferdaous Ben Romdhane [d], Eric M. Gaigneaux [e], Josefine Schnee [f], Edmond Abi-Aad [a]

[a] Unité de Chimie Environnementale et Interactions sur le Vivant, UR 4492, Univ. Littoral Côte d'Opale, 145 avenue Maurice Schumann 59140, Dunkerque, France
[b] Laboratory of Physical Chemistry of Materials (LCPM/PR2N), Lebanese University, Fanar, P.O. Box 90656, Jdeidet El Metn, Lebanon
[c] Department of Chemistry Faculty of Arts and Sciences, University of Balamand, Kelhat, Deir El Balamand, Lebanon
[d] Fédération de Chimie et Matériaux de Paris-Centre (FCMat), Campus Pierre et Marie Curie, 4 Place Jussieu, F-75005 Paris Cedex 05, France
[e] Institute of Condensed Matter and Nanosciences (IMCN), Molecular Chemistry, Materials and Catalysis (MOST), Université catholique de Louvain, Pl. Louis Pasteur 1, L4.01.09, 1348 Ottignies-Louvain-la-Neuve, Belgium
[f] Laboratoire de Réactivité de Surface (LRS), CNRS, Sorbonne Université, Campus Pierre et Marie Curie, 4 Place Jussieu, F-75005 Paris Cedex 05, France

ARTICLE INFO

Keywords:
Layered double hydroxide
Nickel
Methanation
Ultrasound
CO_2 hydrogenation

ABSTRACT

Within the idea to catalyze CO_2 methanation NiMgAl and NiMgAlFe oxides were synthesized by the layered double hydroxide route using co-precipitation and ultrasound-assisted co-precipitation. MgAl and MgAlFe oxides-supported Ni materials prepared by the impregnation method were used as references. Inductively-coupled plasma optical emission spectroscopy, X-ray diffraction, thermal decomposition, H_2-temperature programmed reduction, N_2 physisorption, and transmission electron microscopy were used to characterize the catalysts. NiMgAl prepared using ultrasound-assisted co-precipitation showed the best activity with no deactivation for 40 h under stream. This was attributed mainly to the lower particle size, the higher specific surface area and pore volume as well as the better dispersion of nickel active species at the surface of the concerned materials. In our case, the ultrasound method saves a lot of time during the synthesis process since the maturation phase lasts only 30 min instead of 18 h required for the traditional co-precipitation.

1. Introduction

Global climate change and the gradual depletion of fossil fuels are two of the most pressing issues confronting humanity today [1]. The usage of renewable energy sources (RES), like wind or photovoltaics, is one of the developed solutions [2]. However, they are intermittent [3]. The demand for power from end-users differs with the generation of electricity from RES, implying a potential electrical network imbalance. Power-to-Gas (PtG) is a potential long-term and high-capacity renewable energy storage option. This concept can be an interesting way to use excess electricity to produce H_2 from water electrolysis. However, safety concerns like a wide flammability interval, as well as storage and transportation constraints (e.g., poor energy density, steel embrittlement) limit hydrogen's direct usage [4]. Hydrogen can react with CO_2 stored or emitted according to the Sabatier reaction (1).

$$CO_2 + 4H_2 \rightarrow CH_4 + 2H_2O \quad \Delta H_{298} = -165 kJ.mol^{-1} \tag{1}$$

This reaction enables the production of synthetic natural gas (SNG) methane that has a very high-energy value, can be injected into the natural gas network, and can be directly used as a fuel in the transportation sector [5]. The CH_4 produced offers a potential solution in order to manage fluctuating output of renewable energy and mitigate CO_2 emissions at the same time [6]. However, even though the CO_2 methanation reaction is thermodynamically possible in a practical range of conditions, it remains kinetically limited [7]. An efficient catalyst will increase the rate of the methanation reaction, exhibit high activity, selectivity and stability within an appropriate temperature range, while taking into account economic constraints [8]. Several metals in the

* Corresponding author.
E-mail address: Christophe.poupin@univ-littoral.fr (C. Poupin).

https://doi.org/10.1016/j.cej.2023.145460
Received 17 May 2023; Received in revised form 10 August 2023; Accepted 13 August 2023
Available online 19 August 2023

periodic table's group VIII, including Ni, Co, Fe, Ru, and Rh, are capable of undergoing the methanation process [9–11]. The Earth-abundant Ni-based catalysts have long been the top option for industrial applications [12,13]. Furthermore, many oxides have been studied as potential supports for the methanation reaction such as: CeO_2, TiO_2, MgO, Sm_2O_3, CeO_2/ZrO_2, etc. [13,14]. The stabilization of the active metal on these supports is very crucial to achieve good catalytic activity and stability. However, the exothermic nature of the methanation reaction, results in the thermal aggregation of metallic Ni active sites by hotspots formation in the catalytic bed. As a consequence, the catalysts become less stable. In order to solve these issues, improved properties and well-defined crystalline structures of supports frequently stabilize Ni active sites [15].

In this context, layered double hydroxide structures (LDH) gained a lot of interest as CO_2 methanation catalyst precursors [16]. Indeed, they allow getting catalysts with well crystalline structure, high specific surface area, small metal particle sizes, good thermal stability, and uniform distribution of active sites [17].

The LDH has the general formula: $[(M^{2+})_{1-x}\ (M^{3+})_x(OH)_2](A^{n-})_{x/n}{\cdot}mH_2O$, where M is a metal and A is an anion. The divalent cations M^{2+} can be Mg^{2+} and/or another one, while the trivalent cation M^{3+} can be Al^{3+} and/or something else [18]. Different possibilities are offered for the anions. Since a wide choice of cations and anions is possible, LDH-type materials are promising candidates in heterogeneous catalysis. Therefore, oxides deriving from LDH are often used as active phase supports or as catalysts [19]. Different preparation methods such as co-precipitation, urea hydrolysis and sol–gel methods can be used for the synthesis of the LDH structure [20–22]. Co-precipitation is the most common and generally used process [23]. In order to obtain well-nanocrystallized materials, co-precipitation has been coupled to ultrasound treatment [24]. In addition, the use of ultrasound during the synthesis of catalytic materials showed many advantages over traditional approaches [24]. In this process, acoustic cavitation bubbles collapse into each other, generating high temperatures and pressures developing hot spots [25], resulting in solids with small homogeneous particles and increased specific surface area [26]. Enhanced catalytic activity, selectivity, and stability are all a result of these features [27]. The preparation of LDH using ultrasound routes have received a lot of interest recently due to their efficiency, affordability, simplicity, large specific surface area, adjustable and well-dispersed particle sizes [28–30]. In the present work, nickel was chosen as an active phase due to its high activity and relatively low cost [31]. It can be introduced into the catalysts directly by substituting partially the magnesium or can be added by impregnation on the mixed oxides obtained after the thermal treatment of LDH. Magnesium was used to increase the basicity. Its interaction with the nickel phase is known to lead to its better distribution allowing the capture of CO_2 [32]. In addition, MgO issued from LDH plays an important role as an active site for the activation of CO_2 to form carbonate/hydrocarbonate species that react with hydrogen to form methane [33], while the presence of aluminum ensures a high specific surface area [34,35]. According to the literature, the partial substitution of Al by small quantities of iron is performed to improve the reducibility of nickel species [36]. Thus, to explore the potential of having a high quantity of iron on the reducibility of the catalyst and on the catalytic activity, we chose the composition of 14 wt% of iron.

The objective of this work is the examination and comparison of the catalytic properties in the CO_2 methanation reaction of (NiMgAl, NiMgAlFe) prepared by three different routes (traditional co-precipitation (Cp), ultrasound-assisted co-precipitation (US), and impregnation method (Imp)). The originality of this work is the differentiation of the three above-mentioned preparation methods for the chosen material, a question that has not been addressed before in the context of CO_2 methanation. Furthermore, the US method can be used in different ways (during co-precipitation and in the maturation phase). Contrary to other works, the present paper explores in a rigorous way the operating conditions used in the US method such as ultrasonic power, frequency, time and mode, which can indeed have a significant impact on the synthesis results and consequently on the catalytic performances and allow the comparison of the obtained results with the future studies. These operating conditions are then explained in the experimental section. We also investigated the effect of a high quantity of iron on the catalytic performance.

2. Materials and methods

2.1. Catalysts preparation

Co-precipitation, ultrasound-assisted co-precipitation, and wet impregnation were used to synthesize our catalysts.

First, NiMgAl, NiMgAlFe, MgAl, and MgAlFe layered double hydroxides based on Ni (II), Mg (II), Al (III), and Fe(III) were prepared by co-precipitation thoroughly described in previous studies [37]. The solution containing the desired metal salts is added dropwise to deionized water with the Na_2CO_3 (1 $mol.L^{-1}$) solution, whose pH is adjusted to 9 by a basic NaOH (2 $mol.L^{-1}$) solution. After precipitation, the resulting mixture was stirred for 18 h (maturation step). Then, the mixture was filtered and the precipitate was washed with hot deionized water until a neutral pH was obtained. This washing allows the removal of soluble ions (nitrate, Na^+, …). After having been placed 48 h in the oven at 60 °C, the solid obtained was manually ground to powder in an agate mortar. It should be noted that in our preparations, we took a molar ratio M(II)/M(III) = 3. In all cases, Ni content was 10 wt%. When substituting Al^{3+} by Fe^{3+}, the molar ratio Al/Fe is equal to 1.

Second, regarding the ultrasound-assisted co-precipitation method, the same preparation steps were used, but in the maturation phase instead of lasting for 18 h under stirring, ultrasound irradiations (50 W, pulse mode of 30 s on, 30 s off) were used for 30 min and were carried out on a device driven by a Nextgen frequency generator (SinapTec ultrasonic technology). The volume of the solution was 250 mL. Consequently, the power density was 200 $W.L^{-1}$. The apparatus used in this maturation step consists in an ultrasonic pipe with a volume of 700 mL. It is equipped with eight ultrasonic transducers at 22 kHz with a maximum output power of 400 W.

Third, the wet impregnation method is used to synthesize impregnated catalysts that serve as reference materials. In the same purpose, Ni was impregnated on the mixed oxides derived from MgAl or MgAlFe LDH prepared by the co-precipitation method. In order to obtain the desired materials, all samples were calcined under air at 800 ℃ and reduced under pure hydrogen at 800 ℃. For better comprehension, the synthesis protocols for each of the samples are summarized in Table S1 in the supplementary information sheet.

2.2. Catalysts characterization

The XRD analyses were performed on a BRÜKER D8 diffractometer at room temperature. All samples' scattering intensities were measured with a step size of 0.02° for an integration of 2 s throughout an angular range of $5° < 2\theta < 80°$. Phase identification was accomplished by comparing the diffraction patterns to the common XRD reference patterns in the JCPDS database.

Differential thermal or thermogravimetric analysis (DTA/TG) was carried out on a NETZSCH STA 409 starting from ambient temperature up to 1000 °C (temperature rise of 5 $°C.min^{-1}$) under an airflow of 100 $mL.min^{-1}$. For each analysis, the weight of the test sample was about 10 mg. The software "Universal analysis" is used to process the results obtained.

The actual Ni, Mg, Al and Fe weight contents of the prepared materials were assessed by inductively-coupled plasma optical emission spectroscopy (ICP-OES) with an Agilent 5100 SVDV spectrometer. Samples were mineralized typically as follows. 50 mg of powder was digested with 1 mL of HNO_3 (65% Normatom) at 80–90 °C during 4–6 h and then diluted in 50 mL of ultrapure water. 1 mL of the latter solution was finally diluted by adding HNO_3 (2%) until obtaining a total volume

of 10 mL. For each analysis, three replicates were performed. Blanks were also analyzed to monitor instrument and digestion procedure contamination. Standard solutions were prepared from pluri-elemental and mono-elemental standards (SCP Science) and analyzed for calibration and quality control (drift, reproducibility, and accuracy). The concentration of each element was calculated as the average of the data recorded with 3 or 4 wavelengths.

Temperature programmed reduction (H_2-TPR) experiments were carried out in a Micromeritics Autochem II chemisorption analyzer. About 50 mg of sample were deposited in a quartz tube and pretreated under an argon flow of high purity. This argon flow of 50 mL.min^{-1}, circulates under a temperature ranging from ambient to 150 °C with a rise of 5 °C.min^{-1} under Ar flow. This pretreatment is done to eliminate atmospheric contaminants and water molecules. After this pretreatment, the sample was cooled to room temperature under Ar flow, and then the catalyst is heated to 900 °C with a rise of 5 °C.min^{-1} under a H_2 flow (5 % H_2 in Ar, 50 mL.min^{-1}) followed by naturally cooling down under an Ar flow.

Textural analysis was performed on a Micromeritics 3Flex version 5.03 instrument. The pre-treatment is done under vacuum (continuous draft) at 350 °C for 4 h. The tubes are weighed and then a N_2 physisorption analysis is performed. When the analysis started, the tubes are dipped in a liquid nitrogen bath at −196 ℃. The specific surface is determined by the Brunauer-Emmett-Teller (BET) method. The Barrett-Joyner-Halenda (BJH) method was used to determine pore distribution and pore volume.

Transmission Electron Microscopy (TEM) analyses were carried out using a JEOL 2100Plus UHR microscope operating at 200 kV. The powdered materials were dispersed in ethanol, and then, a drop was evaporated on a carbon-coated copper grid. Mean surface diameters (d=(nidi3)/(nidi2)) were calculated by measuring at least 300 particles for each examined sample from TEM images. Scanning transmission electron microscopy (STEM) images using a high-angle annular dark-field (HAADF) detector were acquired. The image contrast in this mode is strongly correlated with the atomic number: heavier elements contribute to brighter contrast (Z-contrast). Analytic investigations were performed with an energy dispersive X-ray spectrometer (EDX) attached to the microscope column.

2.3. Catalytic tests

The catalytic activity was examined at atmospheric pressure, in a fixed-bed U-shape reactor with a K-type thermocouple at temperatures ranging from 100 ℃ to 400 ℃. 150 mg of catalyst diluted with SiC to achieve a catalytic bed volume of 1 cm^3 was placed in the reactor. Before the test, the catalysts are reduced for 2 h at 800 °C (5 °C/min) under pure hydrogen flow of 20 mL/min. After cooling, the reactor is fed with a gas mixture of $CO_2/H_2/N_2$ with respective volume ratios 10/40/50 with a total flow rate of 100 mL/min (GHSV = 6000 h^{-1}). The reaction temperature is increased from 100 to 400 °C with a rise of 5 °C/min. Each temperature step is maintained for 30 min. A gas chromatography system from Global Analyser Solutions is used to analyze the reagents (CO_2 and H_2) as well as the reaction products (CH_4 and CO). There are two analytical modules in it. The CO_2 gas is separated using the RTQ bond module, while the H_2, CO, and CH_4 gases are separated using the Molsieve 4A module. These compounds are detected using thermal conductivity detectors (TCD_1 and TCD_2). The quantification of the reagents (CO_2 and H_2) and products (CO and CH_4) present in the reaction was done from the values obtained from the chromatograms and the calibrations carried out for each gas. The general formulas used for the calculations of conversions and selectivities are given below (Eqs. (2)–(4)).

- Conversion of CO_2: X_{CO2} (%) $= \frac{nCO2in - nCO2out}{nCO2\ in} \times 100$ (2)
- Selectivity of methane: S_{CH4} (%) $= \frac{nCH4\ formed}{nCO2\ in - nCO2\ out} \times 100$ (3)
- Selectivity of CO: S_{CO} (%) $= \frac{nCO\ formed}{nCO2\ in - nCO2\ out} \times 100$ (4)

nCO_{2in} and nCO_{2out} are respectively the number of moles of CO_2 at the inlet and the outlet of the reactor, $nCH_{4\ formed}$ and $nCO_{\ formed}$ are respectively the number of moles of CH_4 and CO obtained.

3. Results and discussion

3.1. Characterization of the dried samples

The theoretical molar formulas are $Ni_{0.62}Mg_{5.38}Al_2$ LDH, $Ni_{0.62}Mg_{5.38}AlFe$ LDH for the samples prepared by co-precipitation and ultrasound-assisted co-precipitation method for each series, and Mg_6Al_2 LDH, Mg_6AlFe LDH for the support before impregnation. The X-ray diffractograms of the dried samples (before calcination) are shown in Fig. 1. The diffraction lines of LDH structure may be seen in the patterns of all the prepared solids (JCPDS 22-0700).

The diffraction peaks are observed at 2θ of 11.5°, 23.5°, 35.0°, 38.0°, 46.2°, 60.5°, and 61.8° and are respectively indexed to the lattice planes (003), (006), (012), (015), (018), (110), and (113) [38]. Furthermore, aside from the typical LDH lines, no other lines were detected, showing that pure LDH was successfully synthesized in all the solids. Bragg's law, which is provided by the relation in the supplementary material sheet, is used to calculate the inter-planar spacing (d_{hkl}) that corresponds to these peaks. The different cell parameters are given in Table 1. Two parameters "a" and "c" should be evaluated for a LDH structure since it crystallizes in a 3R rhombohedral reticular system [38]. Knowing the lattice planes (*hkl*) and the inter-planar spacing (d_{hkl}), the cell parameters can be determined [24,39] The calculation details of the cell parameters are presented in the supplementary material sheet.

Table 1 lists the crystallographic parameters "a" and "c" of the dried solids determined by XRD measurements. As predicted, there is not any remarkable difference for the "a" parameter for both series of samples, since the crystallographic parameter "a" corresponds to the average cation-cation distance in a hydroxide sheet [39]. Indeed, the values of the radii of Fe^{3+} and Ni^{2+} cations do not differ much from that of Al^{3+} and Mg^{2+}, respectively. Regarding the crystallographic parameter "c", which provides details on the interlayer domain's thickness [40], a decrease of this parameter is noticed when the ultrasound-assisted co-precipitation method is used. The electrostatic interactions between the sheets are thus strengthened leading to a more "compact" LDH structure as the ultrasound is used in the aging phase. These results are in agreement with Macedo et al. [41] who obtained a decrease in the values of the c parameter of NiMgAlCe LDH structure when using ultrasound during the aging phase. The intensity of the indexed peaks decreases when using ultrasound in the aging phase (Fig. 1). The crystallite size of LDHs prepared by ultrasound-assisted co-precipitation is smaller compared to the sample prepared by conventional co-precipitation (Table 1). This effect was also found by Climent et al. [42] who synthesized a series of LDHs using ultrasound in the preparation method. This phenomenon is attributed to the collapse of cavitation bubbles which causes a shock wave and micro-jets on the surface of the particles leading to their breaking [43]. Moreover, the use of ultrasound in the solution results in generation of sufficient nuclei, thereby lowering the supersaturation available for further growth [44]. Thus, ultrasound can be used to control nucleation rates [45]. Furthermore, thermal decomposition analyses were conducted over all the LDH samples. Three endothermic peaks are observed for all solids. Each peak corresponds to a mass loss. The first peak, is due to the loss of physisorbed water from the outer surface of the crystallites. The second peak and the third peak are due to the collapse of the LDH structure and the formation of metal oxides [46]. These three weight loss zones are characteristic of LDH and therefore, in this study, further confirms that LDH structure was achieved for all the samples via different preparation methods. The DTA/TG profiles for all the samples are shown in Fig. S2 in

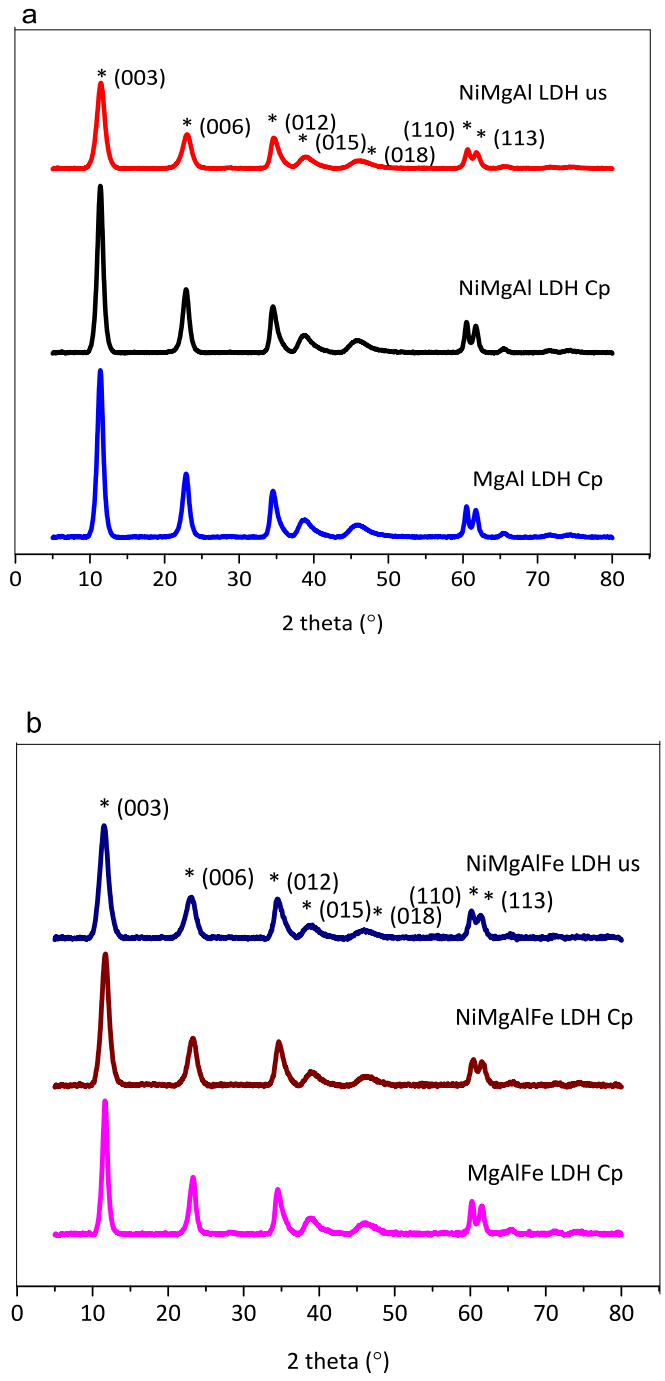

Fig. 1. X-ray diffraction patterns of the dried samples prepared by conventional co-precipitation (Cp) and by co-precipitation assisted by ultrasound (US). (a) MgAl and NiMgAl samples; (b) MgAlFe and NiMgAlFe samples. *: Layered double hydroxide phase (JCPDS N° 22-0700).

Table 1
Cell parameters (a and c) and crystallite size of the dried samples.

Dried solid	a (Å)	c (Å)	Crystallite size (Å)[a]
MgAl LDH Cp	3.06	23.11	104
NiMgAl LDH Cp	3.06	23.19	80
NiMgAl LDH US	3.06	23.09	58
MgAlFe LDH Cp	3.07	22.78	103
NiMgAlFe LDH Cp	3.06	23.11	68
NiMgAlFe LDH US	3.07	22.73	60

[a]Determined by Debye-Scherrer equation.

the supplementary material sheet. Finally, it is worth mentioning that at 800 °C, the LDH structure is destroyed in all our samples. Moreover, from this temperature, the recorded mass loss is negligible. Hence this temperature was chosen for the treatment of the synthesized dried solids.

3.2. Characterization of calcined samples

Fig. 2 shows the X-ray diffractograms of NiMgAl and NiMgAlFe prepared by the three preparation methods used and calcined at 800 °C. The diffractograms of all NiMgAl samples prepared by the three preparation methods were compatible with the following structures: MgO periclase, cubic structure of $MgNiO_2$ or rhombohedral structure of NiO, and spinel oxides $NiAl_2O_4$ and $MgNiO_2$. The X-ray diffractograms for the

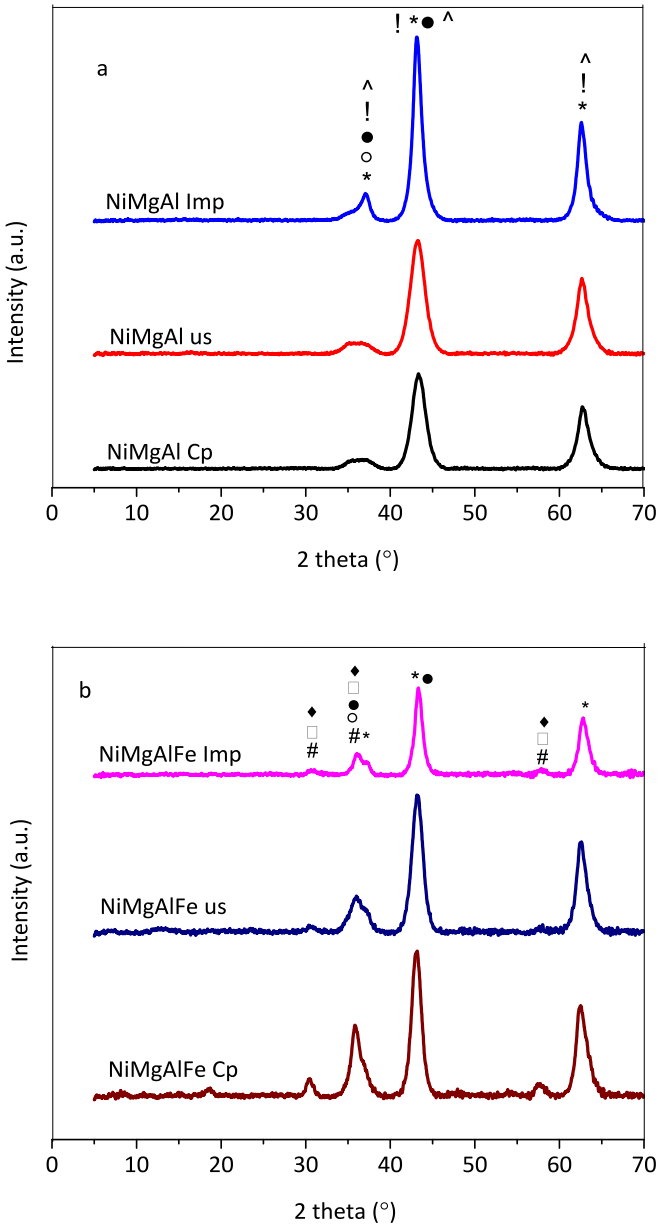

Fig. 2. X-ray diffraction patterns of the calcined samples (a) the NiMgAl samples, (b) the NiMgAlFe, samples. * *MgO periclase JCPDS N° 43-1022,! $MgNiO_2$ cubic JCPDS N° 24-0712,^NiO rhombohedral JCPDS N° 44-1159,* ● *$MgAl_2O_4$ JCPDS N° 75-0713, # Fe_2O_3 Maghemite JCPDS N° 39-1346,* ○ *$NiAl_2O_4$ JCPDS N° 65-3102,* ◆ *Fe_3O_4 Magnetite JCPDS N° 98-3854,* □ *$NiFe_2O_4$ Trevorite JCPDS N° 86-2267.*

NiMgAlFe samples show the presence of new phases corresponding to Fe_2O_3 [47], Fe_3O_4 and $NiFe_2O_4$ [48] at $2\theta = 31°$, 36 and 58°, respectively. Indeed, these samples with a molar ratio $Al^{3+}/Fe^{3+} = 1$ possess a high iron weight content. As a result, the formation of iron oxides may be due to the high iron content present in this solid [47]. Moreover, we note that the change in the preparation method does not affect the formation of crystalline phases.

In heterogeneous catalysis, it is essential to understand the textural characteristics of the resulting oxides. Some catalytic behaviors can be explained by the specific surface area, the pore diameter, the pore volume and the pore type. These characteristics also give us information about the accessibility of the active sites to the reagents. The nitrogen adsorption and desorption isotherms for all the samples are shown in Fig. S3 in the supplementary material sheet. According to the IUPAC classification [49], all our mixed oxides have a type IVa isotherm. Thus, the preparation method has no effect on the type of isotherms. On the other hand, we notice an effect on the type of hysteresis loop. More details concerning this issue are found in the supplementary material sheet. Table 2 shows the textural features and elemental composition of the prepared solids after calcination at 800 °C. The experimental metal loading are very close to the nominal contents in the catalysts with no big difference between the three methods of preparation. The specific surface area and pore volume increase when ultrasonic irradiation was applied during co-precipitation. Ultrasonic irradiation significantly alters the morphology of the particles on the surface. It creates small nanoparticles with a uniform dispersion which led to the increase of the available surface area [50]. However, these values decrease when the active phase (nickel) is added by impregnation, suggesting a clogging of the pores during the addition of the active phase. The specific surface area varies in the following order for the first series: NiMgAl US > NiMgAl Cp > NiMgAl Imp, similarly for the second series, it varies in the following order: NiMgAlFe US > NiMgAlFe Cp > NiMgAl Imp. Moreover, the specific surface area of the iron-containing samples is smaller than that of the iron-free samples regardless of the preparation method used. This may be due to the formation of Fe_2O_3 following the addition of iron. In fact, Fe_2O_3 has a very small specific surface area compared to Al_2O_3 [51]. Regarding the pore diameter, we obtained average diameters between 6 and 12 nm confirming that we obtained mesoporous materials. The use of ultrasound leads to an increase in pore volume, whereas the addition of the active phase by impregnation leads to a decrease in pore volume.

The H_2-TPR profiles of the different NiMgAl and NiMgAlFe solids are shown in Fig. 3. It is to be mentioned that aluminum and magnesium oxides are not reduced in our TPR conditions [52]. First of all, for the samples NiMgAl in Fig. 3 (a), nickel oxide species are reduced at high temperatures (810, 788 and 803 °C, peak 2) as a result of spinel formation [53], which is suggested to occur by the XRD study. For the sample NiMgAl Imp, we note a lower temperature reduction peak (353 °C, peak 1) attributable to nickel oxide weakly interacting with the support [53]. Due to the production of spinel, a characteristic of catalysts formed from hydrotalcite-like precursors, which was evoked in the XRD examination of the calcined samples, the reduction temperatures of NiMgAl mixed oxides are high. This suggests that the nickel ions in the solid matrix have strong interactions, which makes it difficult for NiO species to be reduced at lower temperatures. This difficulty in the reduction of nickel species makes it more resistant towards sintering, resulting in an ability to maintain high dispersion of Ni^0 [48]. The experimental values of H_2 consumptions (presented in Table 3) are close to those obtained theoretically (1.7×10^3 μmol.g^{-1}). For the calculation of the theoretical amount of hydrogen, it was assumed that the nickel is in the form of NiO and has been reduced into Ni^0. The experimental value (1.68×10^3 μmol.g^{-1}) of the amount of hydrogen consumed for both samples NiMgAl Us and NiMgAl Imp are very close to the theoretical one (1.7×10^3 μmol.g^{-1}). This may be due to a better dispersion of the active phase rendering it more accessible to the reducing agent.

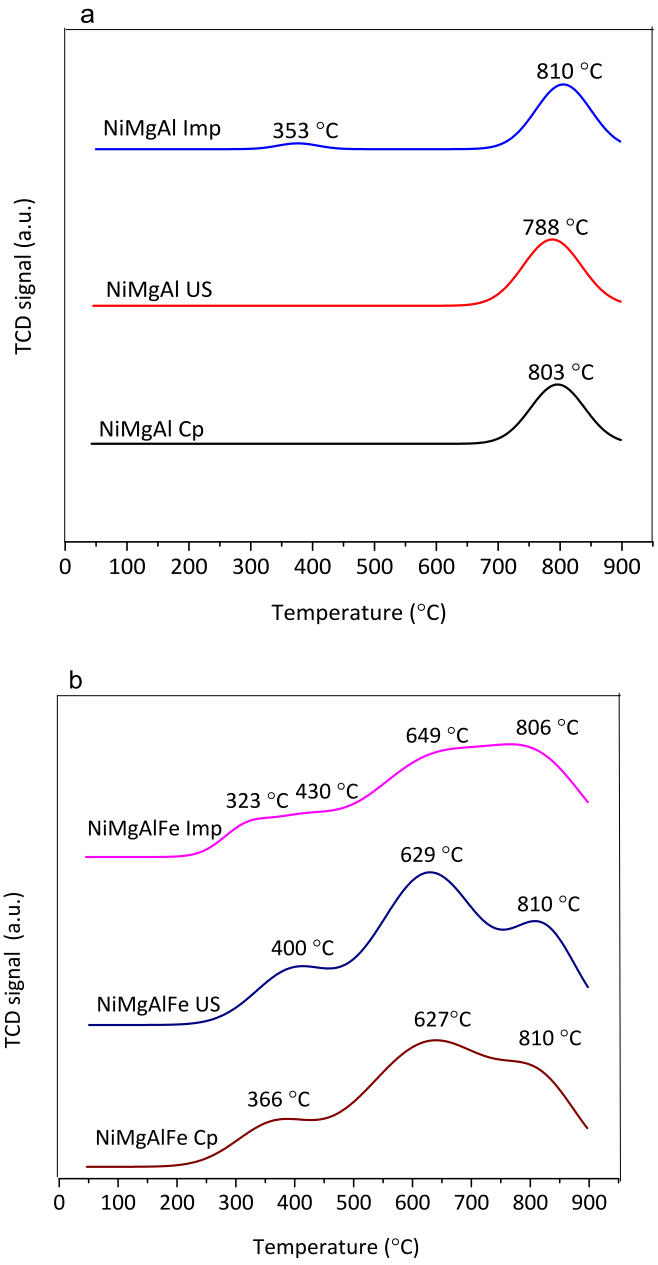

Fig. 3. H_2-temperature programmed reduction (TPR) profiles. (a) NiMgAl samples, (b) NiMgAlFe samples.

Table 2
Specific surface area, pore diameter, pore volume and experimental metal loading of the calcined samples.

Catalyst	S_{BET}[a] ($m^2.g^{-1}$)	Dp[b] (nm)	Vp[b] ($cm^3.g^{-1}$)	Ni[c] (wt%)	Mg[c] (wt%)	Al[c] (wt%)	Fe[c] (Wt %)
NiMgAl Cp	202	9.8	0.44	9.01	28.75	12.91	–
NiMgAl US	232	11.1	0.74	9.28	29.58	13.56	–
NiMgAl Imp	162	6.7	0.38	9.36	30.59	13.01	–
NiMgAlFe Cp	125	12.8	0.46	10.42	24.6	7.39	16.37
NiMgAlFe US	139	13.4	0.55	7.947	25.63	5.81	12.54
NiMgAlFe Imp	120	6.7	0.31	8.705	31.43	7.02	15.29

[a] determined by BET method. [b]determined by BJH method. [c]determined from ICP-OES analysis.

Table 3
Experimental and theoretical H_2 consumption for each peak of the calcined samples.

Sample	Experimental H_2 consumption (10^3 µmol.g^{-1})					Theoretical H_2 consumption (10^3 µmol.g^{-1})			
	Peak 1	Peak 2	Peak 3	Peak 4	Total	Peak2	Peak 3	Peak4 + 1	Total
NiMgAl Cp	–	–	–	1.33	1.33	–	–	1.7	1.7
NiMgAl Us	–	–	–	1.68	1.68	–	–	1.7	1.7
NiMgAl Imp	0.118	–	–	1.55	1.67	–	–	1.7	1.7
NiMgAlFe Cp	–	0.265	0.903	0.270	1.44	0.42	3.38	1.57	5.37
NiMgAlFe Us	–	0.125	1.385	0.43	1.94	0.42	3.38	1.57	5.37
NiMgAlFe Imp	0.019	0.035	0.245	0.299	0.62	0.42	3.38	1.57	5.37

The lower experimental value of hydrogen consumption (1.33 × 10^3 µmol.g^{-1}) of NiMgAl Cp indicates that part of the species has not been completely reduced into metallic ones.

Concerning the H_2-TPR of the iron-containing samples in Fig. 3(b), we note the presence of three reduction peaks for the samples prepared by co-precipitation and ultrasonically assisted co-precipitation and four peaks for the sample prepared by impregnation. Some nickel oxide species are reduced at high temperatures (806–810 °C, peak 4), likely as a result of spinel formation. As for the samples prepared by impregnation, we still notice the reduction peak due to the formation of nickel oxide in weak interaction with the support (323 °C, peak 1). As for the Fe_2O_3 iron oxide species, the peak at 366, 400 or 430 °C (peak 2) is attributed to the reduction of Fe_2O_3 iron species into Fe_3O_4, while the peak at a higher temperature (625–650° C, peak 3) is due to the reduction of Fe_3O_4 species to Fe^0 [54] according to the equations (Eq. S1) presented in the supplementary material sheet. The theoretical value (5.37 × 10^3 µmol.g^{-1}) of hydrogen consumption is higher than those obtained experimentally. These results indicate that some of the species have not been completely reduced into metal. As it can be seen in Table 3, the experimental H_2 consumption of the fourth peak in NiMgAlFe samples is higher of 37% when the ultrasound is used in the maturation phase compared to the traditional co-precipitation, and 30% compared to the impregnation method. These findings confirm that while using ultrasound, the nickel species is more accessible on the surface. Regarding the effect of iron on the reducibility of the nickel species, if the same preparation method is chosen, the H_2 consumption for the reduction of nickel oxide of NiMgAl US is 1.68 × 10^3 µmol.g^{-1} while it is 0.43 × 10^3 µmol.g^{-1} for NiMgAlFe US. This shows that a part of the nickel is covered by iron or that iron takes the place of nickel on the surface.

3.3. Characterization of reduced samples

The calcined samples were reduced at 800 °C during 2 h under pure hydrogen flow. The X-ray diffractograms of all the reduced samples NiMgAl samples (Fig. 4(a)) prepared by the three preparation methods were compatible with the following structures: MgO periclase, and metallic nickel. The X-ray diffractograms for the reduced NiMgAlFe samples (Fig. 4(b)) show the presence of a new phase corresponding to $Fe_{0.64}$-$Ni_{0.36}$, and the absence of metallic nickel. This confirms that a large amount of iron can hinder the formation of metallic nickel (active phase for CO_2 methanation) [48].

Fig. 5 displays representative TEM-measured particle size distributions for the reduced NiMgAl series (the corresponding TEM images of the samples are shown in Figs. S4-S6 in the supplementary material sheet). In the case of the NiMgAl Cp catalyst (Fig. 5(a)), a heterogeneous distribution of nickel particles is observed and their average diameter is 13.1 nm, while it is 8.2 nm for the NiMgAl US catalyst (Fig. 5(b)), and 15.2 nm for NiMgAl Imp catalyst (Fig. 5(c)). These results agree with the crystallite size obtained from XRD (Table 4). This study reveals that the ultrasound assisted co-precipitation method allows decreasing the size of the particles. Similar results were obtained by Kim et al. [55] who confirm that the preparation methods influence the morphology and size of the metal particles. As an example, the scanning transmission electron

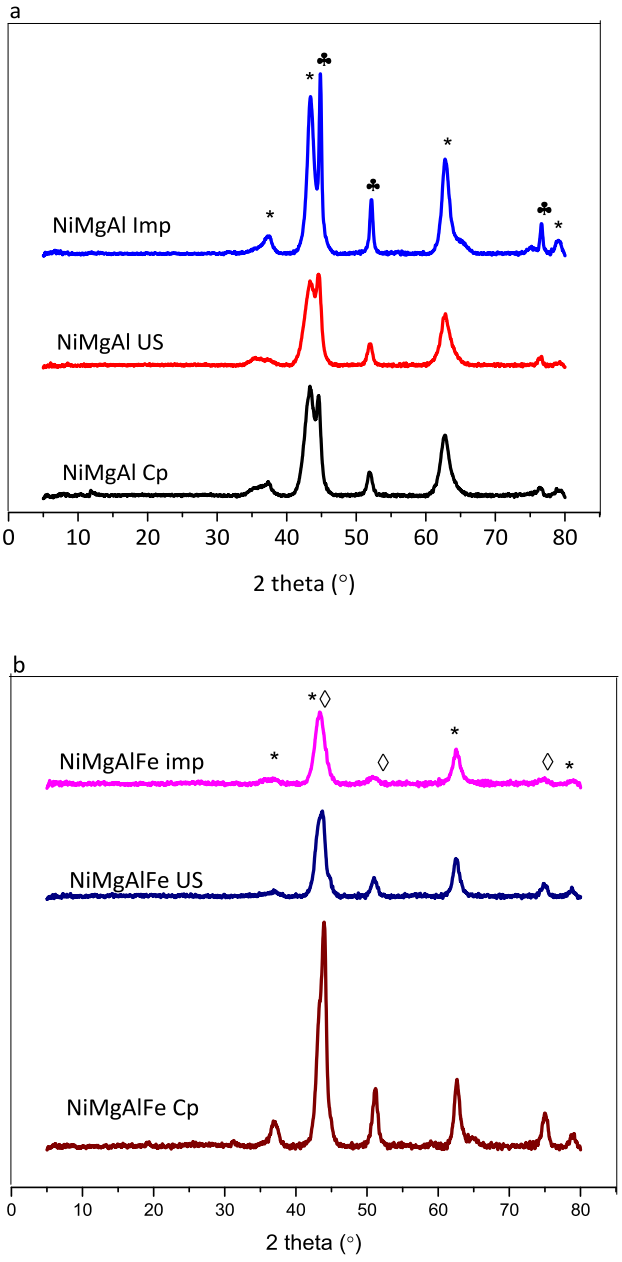

Fig. 4. X-ray diffraction patterns of the reduced samples (a), (b). * MgO periclase JCPDS N° 43-1022, ♣ Ni nickel JCPDS N° 04-0850, ◊ $Fe_{0.64}$-$Ni_{0.36}$ iron nickel JCPDS N° 47-1405.

microscopy (STEM) image of the NiMgAl Cp catalyst shows a good dispersion of heavy nanoparticles (bright spots) on the matrix (Fig. 6). The scanning mode was used to get local and precise chemical analysis at the nanometer scale. However, the results of element mapping suggest

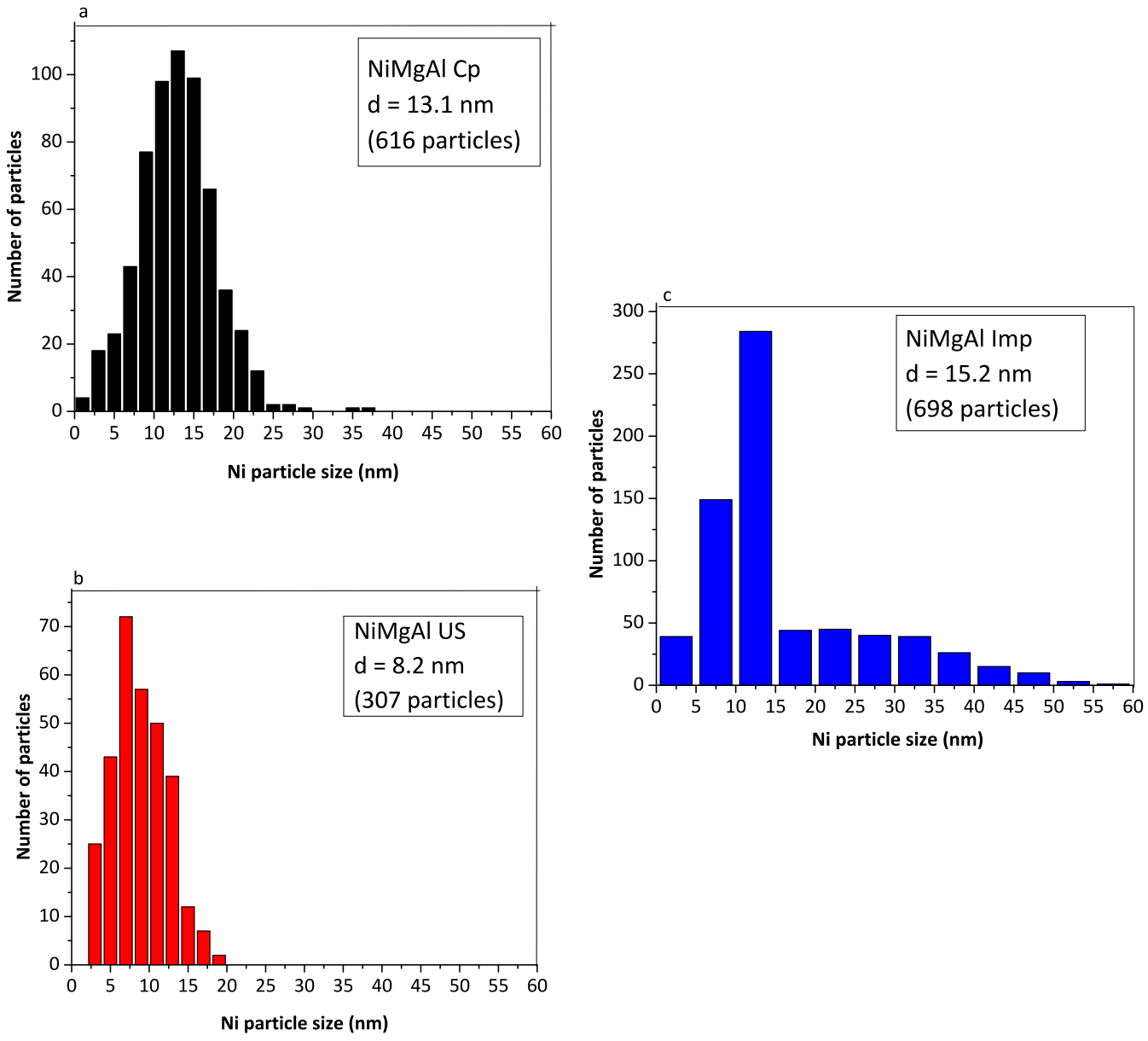

Fig. 5. TEM-measured Ni Particle size distributions for the reduced (a) NiMgAl Cp, (b) NiMgAl US, and (c) NiMgAl Imp.

Table 4
Nickel particle and crystallite size and Ni-Fe crystrallite size.

Catalyst	Ni crystallite size (nm) [a]	Ni particle size (nm)[b]	Ni-Fe crystallite size (nm)[a]
NiMgAl Cp	11.1	13.1	–
NiMgAl US	10.0	8.2	–
NiMgAl Imp	17.4	15.2	–
NiMgAlFe Cp	–	–	11.5
NiMgAlFe US	–	–	10.2
NiMgAlFe Imp	–	–	14.3

[a]Ni and Ni-Fe crystallite size determined by Debye-Scherrer equation based on (200) peak.
[b]Ni particle size determined by TEM analysis, Ni-Fe particle size not measured by TEM analysis.

a good dispersion of the elements (Mg, Al, O, and Ni) and a high homogeneity of them, based on an analysis of several zones, randomly selected. Fig. 7 shows one of these zones. These results confirm the advantages of using LDH precursors in order to obtain homogeneous catalytic materials. They also confirm the identity of nickel particles as observed in Fig. 6. To investigate the crystal structure of the Ni particles, high resolution TEM (HRTEM) was performed. Fig. 8 shows a HRTEM image of an individual particle. Fast Fourier Transform (FFT) on this area reveals the characteristic pattern of the cubic phase for metallic nickel [56].

3.4. Catalytic activity

Fig. 9 shows the catalytic performance in CO_2 conversion over NiMgAl and NiMgAlFe catalysts prepared by co-precipitation, ultrasonic assisted co-precipitation and impregnation. Thermodynamics state that practically total CO_2 conversion is achievable at lower temperatures, and that it declines with rising temperature, as indicated by the dashed line (Fig. 9a, b and d), due to the coexistence of parallel processes which produce undesirable side products, including carbon monoxide. All catalysts show negligible CO_2 conversion at temperatures below 200 °C (Fig. 9a, b and d). The conversion of CO_2 increases with temperature.

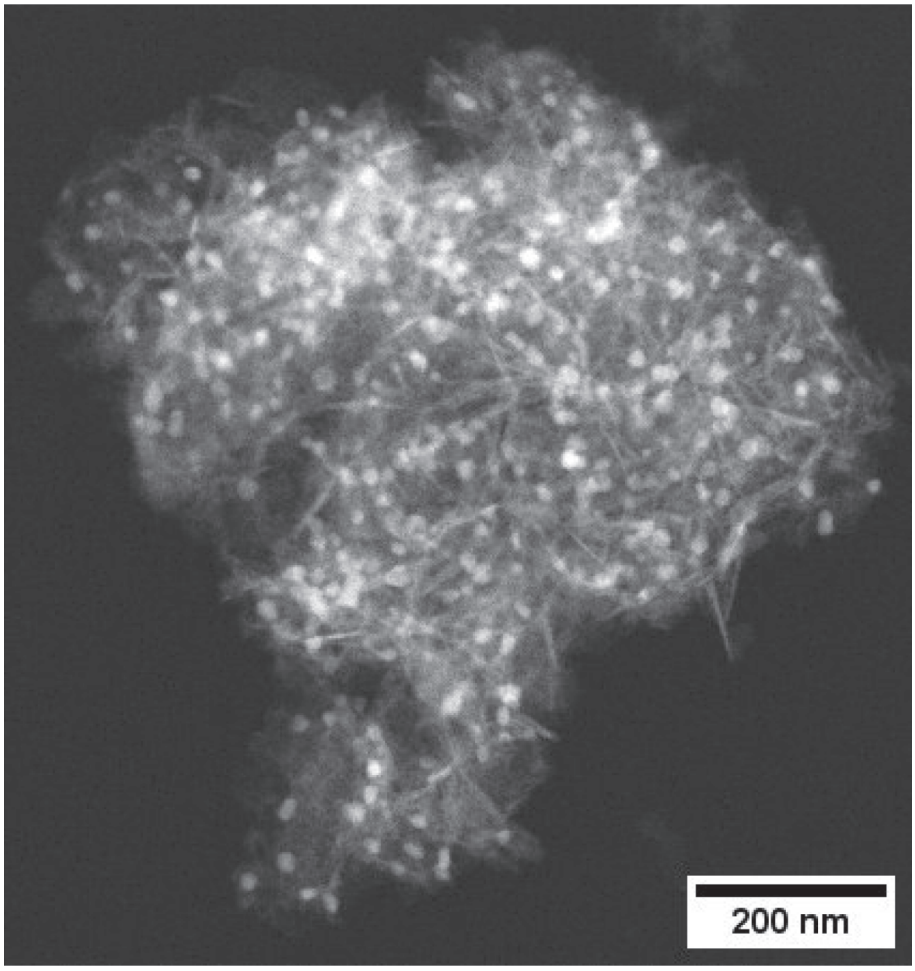

Fig. 6. STEM-HAADF image of NiMgAl Cp.

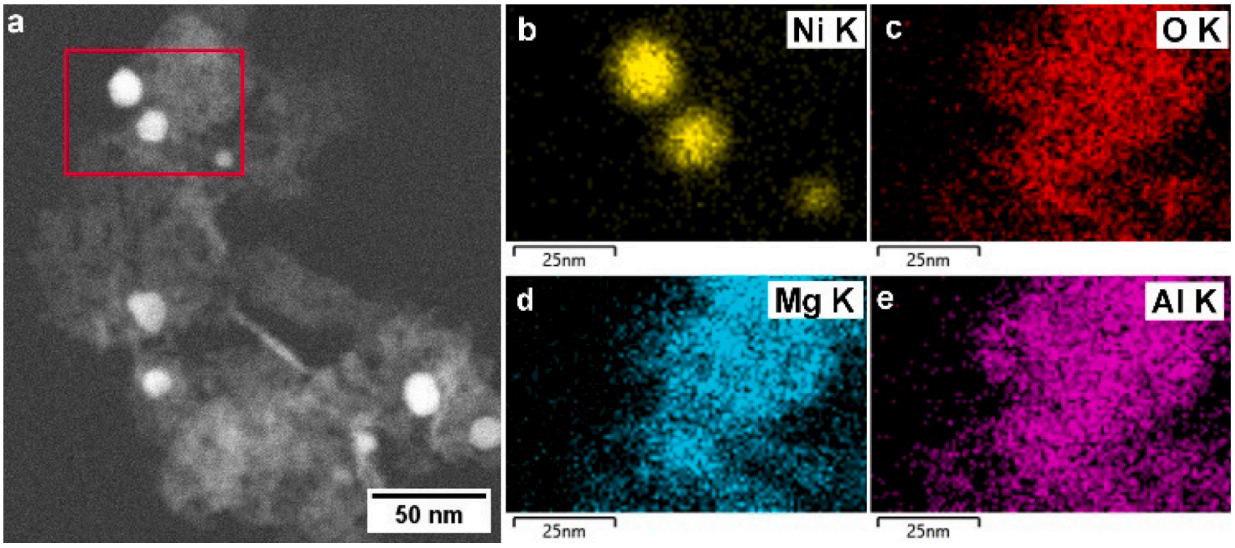

Fig. 7. (a) STEM-HAADF image and corresponding (b-e) STEM-EDX maps.

Indeed, although the methanation reaction is exothermic, the activation of the CO_2 molecule, which is very stable, requires a significant energy input due to its chemical inertia. This energy is provided in thermal form. The conversion of CO_2 varies according to the following order: NiMgAl US > NiMgAl Cp > NiMgAl Imp > NiMgAlFe US > NiMgAlFe Cp > NiMgAlFe Imp. Moreover, all the catalysts of the NiMgAl series are very selective to methane, while the catalysts of the NiMgAlFe series are more selective in CO than in CH_4 (Table 5). This can be related to the presence of a high amount of iron. The NiMgAl US catalyst shows the best conversions amounting to approximately 80% at 400 °C. The

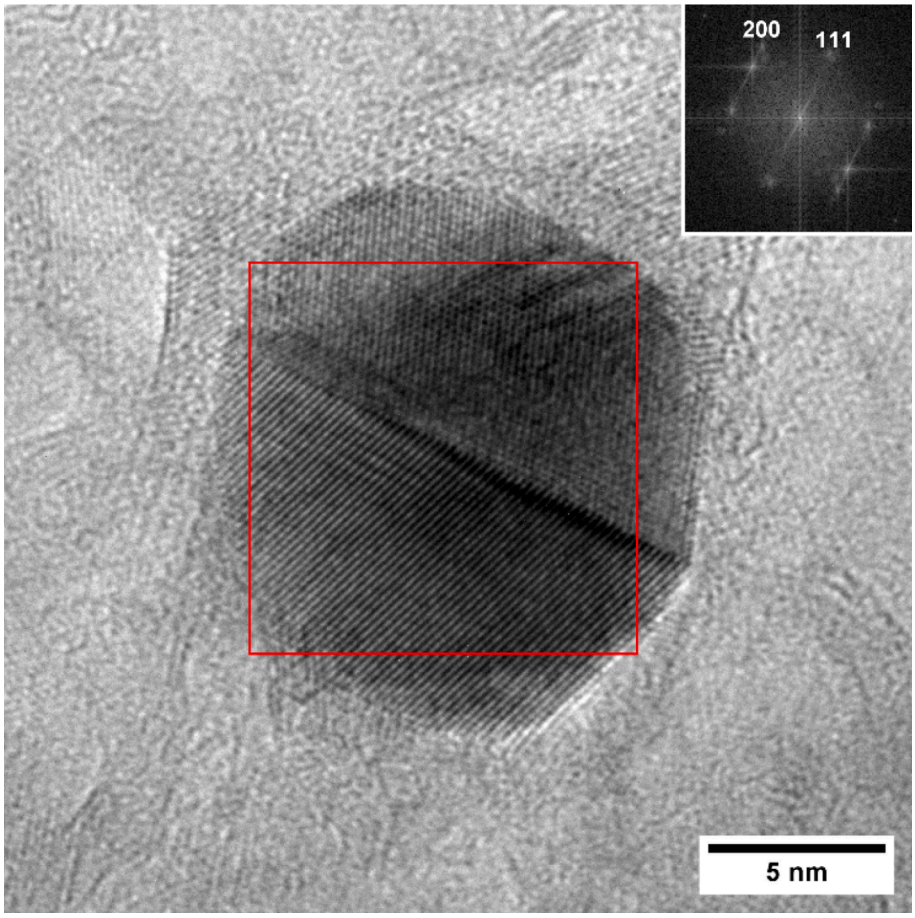

Fig. 8. HRTEM image of a nickel particle of the NiMgAl Cp sample. The inset shows the FFT of the red squared area. (For interpretation of the references to colour in this figure legend, the reader is referred to the web version of this article.)

NiMgAl US catalyst is also very selective towards CH_4 production with selectivity values close to 100% (Table 5). This can be related firstly to the higher specific surface area and larger pore volume, secondly to the higher amount of reducible species as shown by H_2-TPR, and thirdly to the smaller Ni particle size. Regarding the samples containing iron, whatever the preparation method, their CO_2 conversion and selectivity to methane decrease as compared to samples without iron. This may be due to the presence of a large amount of iron in the samples (mass content = 14%). This effect was demonstrated by Pandey et al. [57] who prepared a series of unsupported Ni-Fe bimetallic catalysts. These authors showed that when going from a weight content of 10% Fe to 25%, the CH_4 yield decreased from 80% to 30%. This result would be due to the decrease of the specific surface area and pore volume when the iron content increases. This may also be due to the fact that a high amount of iron promotes the reverse water gas shift reaction (RWGS), leading to high CO selectivity [36]. Fe_2O_3 phase is present in the sample NiMgAlFe as shown in XRD results. Therefore, according to TPR results, the H_2 consumption for the reduction of nickel oxide of NiMgAl US is 1.86×10^3 µmol.g^{-1} while it is 0.43×10^3 µmol.g^{-1} for NiMgAlFe US. We can conclude that a part of the nickel is covered by iron or that iron takes the place of nickel on the surface. In addition, when Fe_2O_3 is present in a catalyst, a different mechanism can occur during the methanation reaction. The formate species is not stable and is decomposed to CO by a reverse water gas shift reaction [14,58–60]. Then, the carbon monoxide might be converted to metal carbide and directly gives C1 to higher hydrocarbons (including olefins and kerosenes) especially at high pressure [58,61]. On the other hand, Ni-based catalysts convert CO_2 to carbonate and then to formate leading to the formation of methane [62]. The H_2-TPR and TEM analysis showed that in NiMgAl US catalyst, the nickel active phase is better dispersed. These results revealed that using ultrasound during the maturation increases the distribution of the active phase. Fig. 9c shows the stability test of NiMgAl US. The latter remains stable for 40 h under stream with no deactivation. A comparison between our best catalyst NiMgAl US and industrial catalyst 50 %Ni/Al_2O_3 is shown in Fig. 9d. At 400 ℃, CO_2 conversion for both catalysts is approximately the same (80%), but the industrial catalyst started to convert CO_2 at lower temperature. However, it is important to mention that our catalyst contains only 10 wt% of nickel while the industrial catalyst contains 50 wt%. This makes our catalyst significantly and advantageously cheaper than the industrial one. In addition, in order to verify the presence of carbon and particle sintering, XRD and thermal analysis were carried out on the samples after catalytic testing. The results of the thermal analysis showed only one exothermic peak attributed to the oxidation of metallic nickel, and the results of the XRD analysis showed that the size of the nickel crystals exhibited the same trend before and after the catalytic test. Thus, we can conclude that for all three preparation methods and for the NiMgAl and NiMgAlFe samples, there is no presence of carbon or particle sintering (results are presented in the supplementary material).

Data from studies that were published on CO_2 methanation in the presence of various catalysts are summarized in Table S2 presented in supplementary material sheet. The catalyst reported in the present study is more effective than most of the already reported catalysts, with a CO_2 conversion of approximately 80% and a CH_4 selectivity of 99.9%. The catalyst 50 %Ni/C catalyst prepared by Gonçalves et al. was evaluated with a GHSV (60000 mL.g^{-1}.h^{-1}), different than that employed in this work (40000 mL.g^{-1}.h^{-1}), and had a CO_2 conversion of 82% at 400 °C [63]. Consequently, a greater Ni concentration is the cause of the

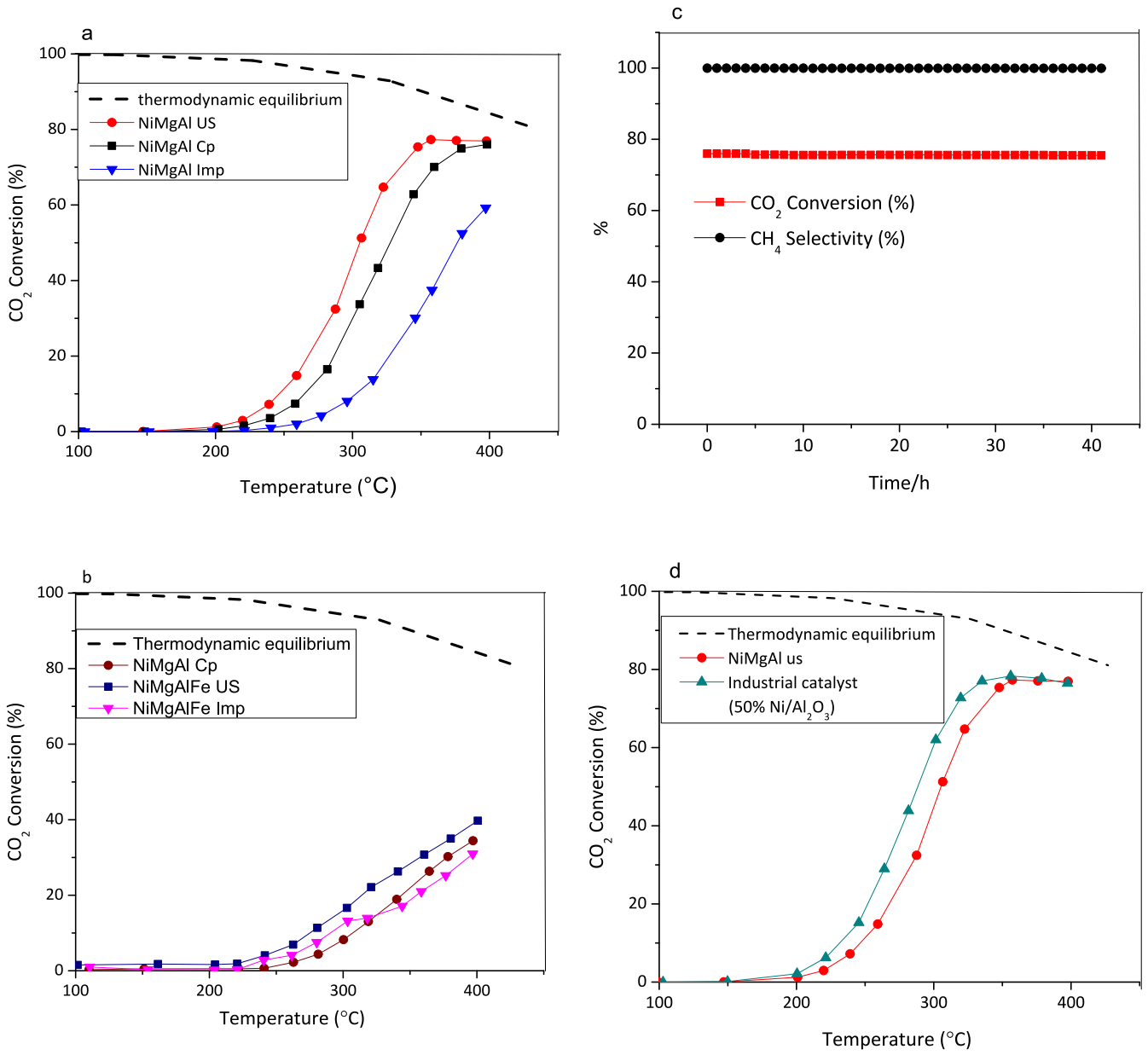

Fig. 9. CO_2 conversion on (a) NiMgAl samples, and (b) NiMgAlFe samples (P = 1 atm, $H_2/CO_2 = 4$ and GHSV = 6000 h^{-1}), (c) long-term stability test over NiMgAl US catalysts at 400 °C ($H_2/CO_2 = 4$, and GHSV = 6000 h^{-1}), and (d) CO_2 conversion on NiMgAl US and industrial catalyst (50 %Ni/Al_2O_3).

Table 5
CH_4 and CO selectivity of all the catalysts at 400 ℃.

Catalyst	CH_4 selectivity (%)	CO selectivity (%)
NiMgAl Cp	99.9	0.1
NiMgAl US	99.9	0.1
NiMgAl Imp	99.6	0.4
NiMgAlFe Cp	40	60
NiMgAlFe US	32	68
NiMgAlFe Imp	49	51
Industrial catalyst (50 %Ni/Al_2O_3)	99.9	0.1

substantially higher CO_2 conversion. On the other hand, the Ni(59%) LDH catalyst prepared by Bette et al. converted 74% of the CO_2 at 350 °C [31] and the 15 %Ni/$Ce_{0.72}Zr_{0.28}O_2$ catalyst prepared by Ocampo et al. [64] converted 82% of CO_2 at 400 ℃ under different GHSV and higher amount of nickel. In addition, the 20 %Ni-3 %Fe/Al_2O_3-ZrO_2 catalyst synthesized by Wu et al. converted 70% of the CO_2 at 400 ℃ [65] with a higher amount of nickel and a small amount of iron. In addition, our catalyst is more effective than those made by Alcalde-Santiago et al. [66], Wierzbicki et al. [67], Dias et al. [68], and Ashok et al. [69] utilizing LaOx, mixed oxides made from LDH, SiO_2, and ZrO_2-CeO_2 as supports, although with the same nickel loading (10 wt%).

This succinct summary was used to compare the NiMgAl US performance to studies that were published in the literature [31,63–71]. Considering crucial factors like metal loading, contact time, and price, our NiMgAl US catalyst prepared by ultrasound-assisted co-precipitation method looks to be very active in the CO_2 methanation reaction.

4. Conclusion

NiMgAl and NiMgAlFe catalysts have been synthesized by three different preparation methods, namely co-precipitation, ultrasound-assisted co-precipitation, and impregnation. They have been characterized and tested for CO_2 methanation. In all the catalysts, 10% of nickel was added either by substituting partially the magnesium or by

impregnation. In order to explore the potential of having a high quantity of iron on the reducibility of the catalyst as well as on the catalytic activity, 14 wt% of iron was substituted for aluminum in order to obtain a molar ratio Al/Fe = 1 in the NiMgAlFe series. Thus, we can conclude that the addition of iron, regardless of the preparation method, decreases CO_2 conversion and methane selectivity. This would be due to the decrease in specific surface area and pore volume following the presence of a large amount of iron in the samples (mass content = 14%), and it could be that a big amount of iron takes the place of active nickel so hindering its activity. In addition, when Fe_2O_3, the formate species is not stable and is decomposed to CO by a reverse water gas shift reaction. However, the NiMgAl Us catalyst was very effective in the CO_2 methanation reaction with only 10 wt% of nickel. It achieved approximately 80% of CO_2 conversion at 400 ℃ with a selectivity close to 100% towards methane production. Furthermore, it demonstrated flawlessly steady performance up to 40 h of operation. Among all the preparation methods used in this study, the ultrasound-assisted co-precipitation is the best method of preparation. First, it saves a lot of time during the synthesis process since ultrasound reduces the required time of maturation from 18 h (traditional co-precipitation) to 30 min. Second, it permits to increase the specific surface area and pore volume, to decrease the Ni particle size, as well as to improve its reducibility. These results confirm that the use of acoustic cavitation is a useful innovative method for obtaining solids with improved catalytic characteristics. We anticipate that this preparation method using specific devices for ultrasonic generation with the possibility of modifying parameters such as power, frequency, time and mode and not using ultrasonic baths whose purpose is to clean the glassware can be used to synthesize different oxides for different applications saving time and energy. It is important to mention that our catalyst shows competitive activity compared to a representative industrial catalyst and it is significantly cheaper than the latter. This suggests that our catalyst offers great potential to be employed in the methanation process.

Declaration of Competing Interest

The authors declare that they have no known competing financial interests or personal relationships that could have appeared to influence the work reported in this paper.

Data availability

Data will be made available on request.

Acknowledgements

The authors would like to thank the Lebanese University and the University of Littoral Coast Opal for their financial support. The TEM microscopes are facilities of the Chemistry and Materials Federation of Paris-Centre (FCMat) and were funded by Sorbonne Université, CNRS and Région Ile de France which are gratefully acknowledged.

Appendix A. Supplementary data

Supplementary data to this article can be found online at https://doi.org/10.1016/j.cej.2023.145460.

References

[1] N.Z. Muradov, T.N. Veziroğlu, “Green” path from fossil-based to hydrogen economy: An overview of carbon-neutral technologies, Int. J. Hydrogen Energy 33 (2008) 6804–6839, https://doi.org/10.1016/j.ijhydene.2008.08.054.
[2] J. Nowotny, T. Bak, D. Chu, S. Fiechter, G.E. Murch, T.N. Veziroglu, Sustainable practices: Solar hydrogen fuel and education program on sustainable energy systems, Int. J. Hydrogen Energy 39 (2014) 4151–4157, https://doi.org/10.1016/j.ijhydene.2013.12.114.
[3] S. Abate, K. Barbera, E. Giglio, F. Deorsola, S. Bensaid, S. Perathoner, R. Pirone, G. Centi, Synthesis, Characterization, and Activity Pattern of Ni-Al Hydrotalcite Catalysts in CO2 Methanation, Ind. Eng. Chem. Res. 55 (2016) 8299–8308, https://doi.org/10.1021/acs.iecr.6b01581.
[4] P. Marocco, E.A. Morosanu, E. Giglio, D. Ferrero, C. Mebrahtu, A. Lanzini, S. Abate, S. Bensaid, S. Perathoner, M. Santarelli, R. Pirone, G. Centi, CO2 methanation over Ni/Al hydrotalcite-derived catalyst: Experimental characterization and kinetic study, Fuel 225 (2018) 230–242, https://doi.org/10.1016/j.fuel.2018.03.137.
[5] E. Giglio, A. Lanzini, M. Santarelli, P. Leone, Synthetic natural gas via integrated high-temperature electrolysis and methanation : Part I — Energy performance, J. Energy Storage. 1 (2015) 22–37, https://doi.org/10.1016/j.est.2015.04.002.
[6] J. Maton, L. Zhao, J. Brouwer, Dynamic modeling of compressed gas energy storage to complement renewable wind power intermittency, Int. J. Hydrogen Energy 38 (2013) 7867–7880, https://doi.org/10.1016/j.ijhydene.2013.04.030.
[7] A.L. Kustov, A.M. Frey, K.E. Larsen, T. Johannessen, J.K. Nørskov, C. H. Christensen, CO methanation over supported bimetallic Ni-Fe catalysts: From computational studies towards catalyst optimization, Appl. Catal. A 320 (2007) 98–104, https://doi.org/10.1016/j.apcata.2006.12.017.
[8] S. Rönsch, J. Schneider, S. Matthischke, M. Schlüter, M. Götz, J. Lefebvre, P. Prabhakaran, S. Bajohr, Review on methanation – From fundamentals to current projects, Fuel 166 (2016) 276–296, https://doi.org/10.1016/j.fuel.2015.10.111.
[9] B. Miao, S.S.K. Ma, X. Wang, H. Su, S.H. Chan, Catalysis mechanisms of CO2 and CO methanation, Catal. Sci. Technol. 6 (2016) 4048–4058, https://doi.org/10.1039/c6cy00478d.
[10] C. Vogt, M. Monai, G.J. Kramer, B.M. Weckhuysen, The renaissance of the Sabatier reaction and its applications on Earth and in space, Nat. Catal. 2 (2019) 188–197, https://doi.org/10.1038/s41929-019-0244-4.
[11] P. Frontera, A. Macario, M. Ferraro, P.L. Antonucci, Supported catalysts for CO2 methanation: A review, Catalysts 7 (2017) 1–28, https://doi.org/10.3390/catal7020059.
[12] A.S. Al-fatesh, S.O. Kasim, A.A. Ibrahim, A.I. Osman, A.E. Abasaeed, H. Atia, U. Armbruster, L. Frusteri, A. Bin Jumah, Y. Mohammed, A.H. Fakeeha, Greenhouse gases utilization via catalytic reforming with Sc promoted Ni /SBA-15, Fuel 330 (2022) 125523, https://doi.org/10.1016/j.fuel.2022.125523.
[13] H.L. Huynh, Z. Yu, CO2 methanation on hydrotalcite-derived catalysts and structured reactors: a review, Energy Technol 8 (5) (2020) 1901475, https://doi.org/10.1002/ente.201901475.
[14] R.A. El-salamony, A.S. Al-fatesh, K. Acharya, A.A.M. Abahussain, A. Bagabas, N. S. Kumar, A.A. Ibrahim, W.U. Khan, R. Kumar, Carbon dioxide valorization into methane using samarium oxide-supported monometallic and bimetallic catalysts Radwa, Catalysts 13 (2023) 113, https://doi.org/10.3390/catal13010113.
[15] W. Li, H. Wang, X. Jiang, J. Zhu, Z. Liu, X. Guo, C. Song, A short review of recent advances in CO2 hydrogenation to hydrocarbons over heterogeneous catalysts, RSC Adv. 8 (2018) 7651–7669, https://doi.org/10.1039/c7ra13546g.
[16] Y.R. Dias, O.W. Perez-Lopez, CO2methanation over Ni-Al LDH-derived catalyst with variable Ni/Al ratio, J. CO2 Util. 68 (2023), 102381, https://doi.org/10.1016/j.jcou.2022.102381.
[17] X. Guo, D. Gao, H. He, A. Traitangwong, M. Gong, V. Meeyoo, Z. Peng, C. Li, Promotion of CO2 methanation at low temperature over hydrotalcite-derived catalysts-effect of the tunable metal species and basicity, Int. J. Hydrogen Energy 46 (1) (2021) 518–530, https://doi.org/10.1016/j.ijhydene.2020.09.193.
[18] H.M.S. Al-Aani, E. Iro, P. Chirra, I. Fechete, M. Badea, C. Negrilă, I. Popescu, M. Olea, I.C. Marcu, CuxCeMgAlO mixed oxide catalysts derived from multicationic LDH precursors for methane total oxidation, Appl. Catal. A 586 (2019) 4–12, https://doi.org/10.1016/j.apcata.2019.117215.
[19] G. Mishra, B. Dash, S. Pandey, Layered double hydroxides : A brief review from fundamentals to application as evolving biomaterials, Appl. Clay Sci. 153 (2018) 172–186, https://doi.org/10.1016/j.clay.2017.12.021.
[20] X. Wang, Z. Yu, L. Ye, M. Zhang, J. Xiong, R. Zhang, X. Li, N. Ji, X. Lu, Layered Double Hydroxide-Derived Bimetallic Ni−Cu Catalysts Prompted the Efficient Conversion of γ-Valerolactone to 2-Methyltetrahydrofuran, ChemCatChem 14 (2022), https://doi.org/10.1002/cctc.202101441.
[21] U. Costantino, F. Marmottini, M. Nocchetti, R. Vivani, New Synthetic Routes to Hydrotalcite-Like Compounds - Characterisation and Properties of the Obtained Materials, Eur. J. Inorg. Chem. (1998), https://doi.org/10.1002/(SICI)1099-0682(199810)1998:10<1439::AID-EJIC1439>3.0.CO;2-1.
[22] F. Prinetto, G. Ghiotti, P. Gra, D. Tichit, Synthesis and characterization of sol - gel Mg / Al and Ni / Al layered double hydroxides and comparison with co-precipitated samples, Microporous Mesoporous Mater. 39 (2000) 229–247, https://doi.org/10.1016/s1387-1811(00)00197-9.
[23] U. Sikander, S. Sufian, M.A. Salam, A review of hydrotalcite based catalysts for hydrogen production systems, Int. J. Hydrogen Energy 42 (2017) 19851–19868, https://doi.org/10.1016/j.ijhydene.2017.06.089.
[24] A. Pérez, J. Lamonier, J. Giraudon, R. Molina, S. Moreno, Catalytic activity of Co – Mg mixed oxides in the VOC oxidation: Effects of ultrasonic assisted in the synthesis, Catal. Today 176 (2011) 286–291, https://doi.org/10.1016/j.cattod.2010.11.088.
[25] M. Shari, M. Haghighi, M. Abdollahifar, Hydrogen production via reforming of biogas over nanostructured Ni/Y catalyst : Effect of ultrasound irradiation and Ni-content on catalyst properties and performance, Mater. Res. Bull. 60 (2014) 328–340, https://doi.org/10.1016/j.materresbull.2014.07.027.
[26] S. Allahyari, M. Haghighi, A. Ebadi, S. Hosseinzadeh, Ultrasound assisted co-precipitation of nanostructured CuO – ZnO – Al2O3 over HZSM-5: Effect of precursor and irradiation power on nanocatalyst properties and catalytic performance for direct syngas to DME, Ultrason. - Sonochem. 21 (2014) 663–673, https://doi.org/10.1016/j.ultsonch.2013.09.014.
[27] Y. Vafaeian, M. Haghighi, S. Aghamohammadi, Ultrasound assisted dispersion of different amount of Ni over ZSM-5 used as nanostructured catalyst for hydrogen

production via CO 2 reforming of methane, Energy Convers. Manag. 76 (2013) 1093–1103, https://doi.org/10.1016/j.enconman.2013.08.010.
[28] M. Dinari, S. Mallakpour, Ultrasound-assisted one-pot preparation of organo-modified nano-sized layered double hydroxide and its nanocomposites with polyvinylpyrrolidone, J. Polym. Res. 21 (2014) 350, https://doi.org/10.1007/s10965-013-0350-y.
[29] S.R. Yahyavi, M. Haghighi, S. Shafiei, M. Abdollahifar, F. Rahmani, Ultrasound-assisted synthesis and physicochemical characterization of Ni-Co/Al2O3-MgO nanocatalysts enhanced by different amounts of MgO used for CH4/CO2 reforming, Energy Convers. Manag. 97 (2015) 273–281, https://doi.org/10.1016/j.enconman.2015.03.064.
[30] L. Yosefi, M. Haghighi, S. Allahyari, S. Ashkriz, Effect of ultrasound irradiation and Ni-loading on properties and performance of CeO2-doped Ni/clinoptilolite nanocatalyst used in polluted air treatment, Process Saf. Environ. Prot. 95 (2015) 26–37, https://doi.org/10.1016/j.psep.2015.02.006.
[31] N. Bette, J. Thielemann, M. Schreiner, F. Mertens, Methanation of CO2 over a (Mg, Al)Ox Supported Nickel Catalyst Derived from a (Ni, Mg, Al) -Hydrotalcite-like Precursor, Chemcatchem. Commun. 8 (18) (2016) 2903–2906, https://doi.org/10.1002/cctc.201600469.
[32] D.P. Debecker, E.M. Gaigneaux, G. Busca, Exploring, tuning, and exploiting the basicity of hydrotalcites for applications in heterogeneous catalysis, Chem. - A Eur. J. 15 (2009) 3920–3935, https://doi.org/10.1002/chem.200900060.
[33] H. Liu, D. Wierzbicki, R. Debek, M. Motak, T. Grzybek, P. Da Costa, M.E. Gálvez, La-promoted Ni-hydrotalcite-derived catalysts for dry reforming of methane at low temperatures, Fuel 182 (2016) 8–16, https://doi.org/10.1016/j.fuel.2016.05.073.
[34] Y. Sun, J. Zhou, W. Cai, R. Zhao, J. Yuan, Hierarchically porous NiAl-LDH nanoparticles as highly efficient adsorbent for p-nitrophenol from water, Appl. Surf. Sci. 349 (2015) 897–903, https://doi.org/10.1016/j.apsusc.2015.05.041.
[35] F.B.D. Saiah, B.L. Su, N. Bettahar, Nickel-iron layered double hydroxide (LDH): Textural properties upon hydrothermal treatments and application on dye sorption, J. Hazard. Mater. 165 (2009) 206–217, https://doi.org/10.1016/j.jhazmat.2008.09.125.
[36] D. Wierzbicki, M.V. Moreno, S. Ognier, M. Motak, T. Grzybek, P. Da Costa, M. E. Gálvez, Ni-Fe layered double hydroxide derived catalysts for non-plasma and DBD plasma-assisted CO2 methanation, Int. J. Hydrogen Energy 45 (2020) 10423–10432, https://doi.org/10.1016/j.ijhydene.2019.06.095.
[37] C. Tanios, S. Bsaibes, C. Gennequin, M. Labaki, F. Cazier, S. Billet, H.L. Tidahy, B. Nsouli, A. Aboukaïs, E. Abi-Aad, Syngas production by the CO2 reforming of CH4 over Ni–Co–Mg–Al catalysts obtained from hydrotalcite precursors, Int. J. Hydrogen Energy 42 (2017) 12818–12828, https://doi.org/10.1016/j.ijhydene.2017.01.120.
[38] D. Li, M. Koike, J. Chen, Y. Nakagawa, K. Tomishige, Preparation of Ni-Cu/Mg/Al catalysts from hydrotalcite-like compounds for hydrogen production by steam reforming of biomass tar, Int. J. Hydrogen Energy 39 (2014) 10959–10970, https://doi.org/10.1016/j.ijhydene.2014.05.062.
[39] C. Rizescu, C. Sun, I. Popescu, A. Urdă, P. Da Costa, I.C. Marcu, Hydrodeoxygenation of benzyl alcohol on transition-metal-containing mixed oxides catalysts derived from layered double hydroxide precursors, Catal. Today 366 (2021) 235–244, https://doi.org/10.1016/j.cattod.2020.04.055.
[40] R. Mrad, R. Cousin, C. Poupin, A. Aboukaïs, S. Siffert, Propene oxidation and NO reduction over MgCu-Al(Fe) mixed oxides derived from hydrotalcite-like compounds, Catal. Today 257 (2015) 98–103, https://doi.org/10.1016/j.cattod.2015.02.020.
[41] O.R. Macedo, N.F.P. Ribeiro, C.A.C. Perez, M. Schmal, M.M.V.M. Souza, Incorporation of cerium ions by sonication in Ni – Mg – Al layered double hydroxides, Appl. Clay Sci. 48 (2010) 542–546, https://doi.org/10.1016/j.clay.2010.02.015.
[42] M.J. Climent, A. Corma, S. Iborra, K. Epping, A. Velty, Increasing the basicity and catalytic activity of hydrotalcites by different synthesis procedures, J. Catal. 225 (2004) 316–326, https://doi.org/10.1016/j.jcat.2004.04.027.
[43] R. Ambati, P.R. Gogate, Ultrasound assisted synthesis of iron doped TiO2 catalyst, Ultrason. Sonochem. 40 (2018) 91–100, https://doi.org/10.1016/j.ultsonch.2017.07.002.
[44] R. Prasad, S.V. Dalvi, Sonocrystallization: Monitoring and controlling crystallization using ultrasound, Chem. Eng. Sci. 226 (2020), 115911, https://doi.org/10.1016/j.ces.2020.115911.
[45] K. Seo, S. Suzuki, T. Kinoshita, I. Hirasawa, Effect of Ultrasonic Irradiation on the Crystallization of Sodium Acetate Trihydrate Utilized as Heat Storage Material, Chem. Eng. Technol. 35 (2012) 1013–1016, https://doi.org/10.1002/ceat.201100680.
[46] S. Naseem, B. Gevers, R. Boldt, F.J.W.J. Labuschagné, A. Leuteritz, Comparison of transition metal (Fe Co, Ni, Cu, and Zn) containing tri-metal layered double hydroxides (LDHs) prepared by urea hydrolysis, R. Soc. Chem. Adv. 9 (2019) 3030–3040, https://doi.org/10.1039/c8ra10165e.
[47] D.C. Carvalho, N.A. Ferreira, J.M. Filho, O.P. Ferreira, J.M. Soares, A.C. Oliveira, Ni – Fe and Co – Fe binary oxides derived from layered double hydroxides and their catalytic evaluation for hydrogen production, Catal. Today 250 (2015) 155–165, https://doi.org/10.1016/j.cattod.2014.08.010.
[48] C. Mebrahtu, F. Krebs, S. Perathoner, S. Abate, G. Centi, R. Palkovits, Hydrotalcite based Ni – Fe /(Mg, Al)Ox catalysts for improved CO dissociation, basicity, and particle size, Catal. Sci. Technol. 8 (2018) 1016–1913, https://doi.org/10.1039/C7CY02099F.
[49] F. Rouquerol, J. Rouquerol, K.S.W. Sing, P. Lewellyn, G. Maurin, Adsorption by Powders and Porous Solids: Principle, Methodology and Applications, Elsevier, 2013.
[50] T. Hosseini, M. Haghighi, H. Ajamein, Fuel cell-grade hydrogen production from methanol over sonochemical coprecipitated copper based nanocatalyst: Influence of irradiation power and time on catalytic properties and performance, Energy Convers. Manag. 126 (2016) 595–607, https://doi.org/10.1016/j.enconman.2016.07.056.
[51] J. Kirchner, J.K. Anolleck, H. Lösch, S. Kureti, Methanation of CO2 on iron based catalysts, Appl. Catal. B Environ. 223 (2018) 47–59, https://doi.org/10.1016/j.apcatb.2017.06.025.
[52] R. Dębek, K. Zubek, M. Motak, M.E. Galvez, P. Da Costa, T. Grzybek, Ni-Al hydrotalcite-like material as the catalyst precursors for the dry reforming of methane at low temperature, Comptes Rendus Chim. 18 (2015) 1205–1210, https://doi.org/10.1016/j.crci.2015.04.005.
[53] H. Nguyen-Phu, T. Kim, Y. Kim, K.H. Kang, H. Cho, J. Kim, I. Ro, Role of phase in NiMgAl mixed oxide catalysts for CO2 dry methane reforming (DRM), Catal. Today 411-412 (2023) 113894, https://doi.org/10.1016/j.cattod.2022.08.036.
[54] E. Amini, M. Rezaei, M. Sadeghinia, Low temperature CO oxidation over mesoporous CuFe2O4 nanopowders synthesized by a novel sol-gel method, Cuihua Xuebao/Chinese, J. Catal. 34 (2013) 1762–1767, https://doi.org/10.1016/s1872-2067(12)60653-6.
[55] J. Kim, D. Jin, T. Park, K. Kim, Effect of metal particle size on coking during CO2 reforming of CH4 over Ni – alumina aerogel catalysts, Appl. Catal. A 197 (2000) 191–200, https://doi.org/10.1016/S0926-860X(99)00487-1.
[56] L. Lin, C.A. Gerlak, C. Liu, J. Llorca, S. Yao, N. Rui, F. Zhang, Z. Liu, S. Zhang, K. Deng, C.B. Murray, J.A. Rodriguez, S.D. Senanayake, Effect of Ni particle size on the production of renewable methane from CO2 over Ni/CeO2 catalyst, J. Energy Chem. 61 (2021) 602–611, https://doi.org/10.1016/j.jechem.2021.02.021.
[57] D. Pandey, K. Ray, R. Bhardwaj, S. Bojja, K.V.R. Chary, G. Deo, Promotion of unsupported nickel catalyst using iron for CO2 methanation, Int. J. Hydrogen Energy 43 (2018) 4987–5000, https://doi.org/10.1016/j.ijhydene.2018.01.144.
[58] G. Kishan, M. Lee, S. Nam, M. Choi, K. Lee, The catalytic conversion of CO2 to hydrocarbons over Fe-K supported on Al2O3-MgO mixed oxides, Catal. Letters. 56 (1998) 215–219, doi: 10.1023/A:1019089919614.
[59] F.A. De la Rosa-Priego, E.D. Gutierrez-López, T.A. Zepeda, M. Acosta-Alejandro, A. M. Venezia, S. Fuentes-Moyado, B. Pawelec, J.N. Díaz-De-León, Enhanced CO2 Hydrogenation to C2+ Hydrocarbons over Mesoporous x%Fe2O3–Al2O3 Catalysts, Ind. Eng. Chem. Res. 60 (2021) 18660–18671, https://doi.org/10.1021/acs.iecr.1c01453.
[60] J. Weiß, Q. Yang, U. Bentrup, E.V. Kondratenko, A. Brückner, C. Kubis, Operando DRIFT and In situ Raman Spectroscopic Studies on Aspects of CO2 Fischer-Tropsch Synthesis Catalyzed by Bulk Iron Oxide-Based Catalysts, ChemCatChem 14 (22) (2022), https://doi.org/10.1002/cctc.202200577.
[61] J. Kim, S. Lee, M. Kang, K. Lee, M. Choi, Y. Kang, Promotion of CO2 Hydrogenation to Hydrocarbons in Three-Phase Catalytic (Fe-Cu-K-Al) Slurry Reactors, Korean J. Chem. Eng. 20 (2003) 967–972, https://doi.org/10.1007/BF02697307.
[62] L. Deng, X. Liu, R. Wang, C. Wang, G. Zhou, Unsupported Ni-Co alloy as efficient catalysts for CO 2 methanation, J. Alloy. Compd. 918 (2022), 165472, https://doi.org/10.1016/j.jallcom.2022.165472.
[63] L.P.L. Gonçalves, A. Serov, G. Mccool, M. Dicome, O.I. Lebedev, M.F.R. Pereira, Y. V. Kolen, New Opportunity for Carbon-Supported Ni-based Electrocatalysts : Gas-Phase CO2 Methanation, ChemCatChem 13 (2021) 4770–4779, https://doi.org/10.1002/cctc.202101284.
[64] F. Ocampo, B. Louis, A.C. Roger, Methanation of carbon dioxide over nickel-based Ce0.72Zr0.28O2 mixed oxide catalysts prepared by sol-gel method, Appl. Catal. A 369 (2009) 90–96, https://doi.org/10.1016/j.apcata.2009.09.005.
[65] Y. Wu, J. Lin, Y. Xu, G. Ma, J. Wang, M. Ding, Transition Metals Modified Ni-M (M=Fe Co, Cr and Mn) Catalysts Supported on Al2O3-ZrO2 for Low-Temperature CO2 Methanation, ChemCatChem 12 (13) (2020) 3553–3559, doi: 10.1002/cctc.202000399..
[66] V. Alcalde-Santiago, A. Davó-Quiñonero, D. Lozano-Castelló, A. Quindimil, U. De-La-Torre, B. Pereda-Ayo, J.A. González-Marcos, J.R. González-Velasco, A. Bueno-López, Ni/LnOx Catalysts (Ln=La, Ce or Pr) for CO2 Methanation, ChemCatChem 11 (2019) 810–819, https://doi.org/10.1002/cctc.201801585.
[67] D. Wierzbicki, R. Baran, R. Dębek, M. Motak, T. Grzybek, M.E. Gálvez, P. Da Costa, The influence of nickel content on the performance of hydrotalcite-derived catalysts in CO2 methanation reaction, Int. J. Hydrogen Energy 42 (2017) 23548, https://doi.org/10.1016/j.ijhydene.2017.02.148.
[68] Y.R. Dias, O.W. Perez-Lopez, Carbon dioxide methanation over Ni-Cu/SiO2 catalysts, Energy Convers. Manag. 203 (2020), 112214, https://doi.org/10.1016/j.enconman.2019.112214.
[69] J. Ashok, M.L. Ang, S. Kawi, Enhanced activity of CO2 methanation over Ni/CeO2-ZrO2 catalysts: Influence of preparation methods, Catal. Today 281 (2017) 304–311, https://doi.org/10.1016/j.cattod.2016.07.020.
[70] M.C. Bacariza, I. Graça, S.S. Bebiano, J.M. Lopes, C. Henriques, Micro- and mesoporous supports for CO2 methanation catalysts: A comparison between SBA-15, MCM-41 and USY zeolite, Chem. Eng. Sci. 175 (2018) 72–83, https://doi.org/10.1016/j.ces.2017.09.027.
[71] Q. Liu, Y. Tian, One-pot synthesis of NiO/SBA-15 monolith catalyst with a three-dimensional framework for CO2 methanation, Int. J. Hydrogen Energy 42 (2017) 12295–12300, https://doi.org/10.1016/j.ijhydene.2017.02.070.